Fundamental Investigation of Oxygen Reduction Reaction on Rhodium Sulfide-Based Chalcogenides

Joseph M. Ziegelbauer,[†,‡] Daniel Gatewood,[§] Andrea F. Gullá,[||] Maxime J.-F. Guinel,[⊥] Frank Ernst,[⊥] David E. Ramaker,[§] and Sanjeev Mukerjee*[,‡]

Department of Chemistry and Chemical Biology, Northeastern University, Boston, Massachusetts 02115, Department of Chemistry, The George Washington University, Washington, D.C. 20375, De Nora Research and Development Division, 625 East Street, Fairport Harbor, Ohio 44077, and Department of Materials Science and Engineering, Case Western Reserve University, Cleveland, Ohio 44106

Received: October 21, 2008; Revised Manuscript Received: January 5, 2009

Synchrotron-based X-ray absorption spectroscopy (XAS), including the surface-specific ΔXANES technique, is used to investigate the active reaction site for water activation and the oxygen reduction reaction (ORR) on the novel, mixed-phase chalcogenide electrocatalyst Rh_xS_y/C (De Nora). The specific adsorption of water, OH, and O as a function of overpotential is reported. This study builds on a prior communication based solely on interpreting the XAS spectra of Rh_xS_y with respect to the metallic Rh_3S_4 phase. Here, a more extensive overview of the electrocatalysis is provided on Rh_xS_y/C, the thermally grown Rh_2S_3/C and Rh_3S_4/C preferential phases and a standard 30 wt % Rh/C electrocatalyst, including results obtained by X-ray diffraction (XRD), XAS, high-resolution transmission electron imaging, microanalysis, and electrochemical investigations. Heating of the Rh_xS_y catalysts to prepare the two preferential phases causes Rh segregation and the formation of Rh metal particles, and immersion in TFMSA causes S dissolution and the formation of a Rh skin on the Rh_xS_y samples. It is shown that some Rh−Rh interactions are needed to carry out the ORR. This is present on the Rh_6 moieties in both the Rh_3S_4 and Rh_xS_y catalysts, but a partial Rh skin (present from acid dissolution) is also contributing to the ORR observed on Rh_xS_y. This to our knowledge is the first time a reaction site in a multiphase inorganic framework structure has been investigated in terms of electrocatalytic pathway for oxygen reduction.

1. Introduction

Attempts at finding alternatives to Pt for catalysis of the oxygen reduction reaction (ORR) in acidic environments have included a wide variety of geometric structures, some fundamentally different from the conventional metal surfaces in highly dispersed Pt (i.e., with typical particle sizes in the range of 1.5−8 nm). Extensive studies have been previously conducted on metal alloys with and without enrichment of alloying elements on the surface.[1,2] These more conventional structures have been relatively easy to characterize. However, the more complex alternative structures, such as those involving inorganic complexes and organo-metallics,[3−5] have proven to be more difficult to characterize, particularly in terms of our understanding of the nature of the reaction centers and the electrocatalytic pathways as a function of overpotential.

Some of the most promising alternative systems for ORR are based on transition metal chalcogenides.[6,7] Several of these systems exhibit reasonably high performances (e.g., Ru_xSe_y/C $i_0 = 2.22 \times 10^{-5}$ A m^{-2}, 0.5 M H_2SO_4),[8,9] and many have been reported to be relatively unaffected by typical poisons of Pt electrocatalysts, such as methanol[10−12] and halides.[13] However, a full characterization of the pertinent structure/property relationships that give rise to their performance and depolarization has proven to be difficult. This arises in part because the synthetic methods[14,15] typically involve mixing nanoparticles of unreduced metal or metal carbonyl complexes with the elemental chalcogen in an organic solvent, and tend to produce small, amorphous clusters.[16,17]

The limited crystallinity of these alternate catalysts almost immediately rules out powder X-ray diffraction as a characterization technique. In addition, many other techniques (e.g., XPS, HREELS, LEEDS, etc.) can provide detailed information regarding the structure of amorphous materials, but are limited by both their ex situ nature and ultrahigh vacuum (UHV) requirements. FTIR techniques can be applied to study certain species on the catalyst surface (CO, CO_2, HCOOH, etc.) but cannot provide information regarding O and OH adsorption nor the specific adsorption sites of the active metal.[18,19] Additionally, specialized IR techniques, such as subtractively normalized interference FTIR (SNIFTIRS), have been employed to study compact adlayers of adsorbed CO on Pt and Pt-alloy catalysts.[20−22] Unfortunately, a surface with a mirror finish is required, and thus it is not yet possible to probe catalysts supported on porous carbon substrates with this technique.[23]

In light of these limitations, synchrotron X-ray absorption spectroscopy (XAS) is particularly promising. In addition to being a short-range order technique, XAS is element specific, and, as a core level spectroscopy, inherently quantitative. The use of high-intensity synchrotron radiation eliminates the need for high vacuum conditions, and allows for the investigation of electrocatalysts *in operando*[24] via specially designed electrochemical cells.[25,26] XAS is, however, a bulk-averaging technique.

* To whom correspondence should be addressed. Phone: (617) 373-2382. Fax: (617) 373-8949. E-mail: s.mukerjee@neu.edu.
[†] Current Address: General Motors R&D Center, MC: 480-102-000, 30500 Mound Road, Warren, MI 48090.
[‡] Northeastern University.
[§] The George Washington University.
[||] De Nora Research and Development Division.
[⊥] Case Western Reserve University.

10.1021/jp809296x CCC: $40.75
Published on Web 04/03/2009

Thus, while the morphologies of the examined catalysts could be ascertained from traditional EXAFS analysis (coordination number, Debye−Waller factor, and bond distances) the adsorbate species could not traditionally be resolved with the exception of clusters where the surface-to-bulk atomic ratio is favorable. This is possible only in a narrow particle size range of up to 4 nm. This limitation was finally eliminated with the advent of the $\Delta\mu$ analysis technique.[27,28] By performing a careful normalization of X-ray absorption spectroscopy near-edge structure (XANES) spectra and then subtracting successive signals from a reference spectrum (such as those on clean surfaces absent adsorbed moieties), the bulk information (traditional metal−metal and metal−oxide interactions) is effectively removed from the signal. The remaining data then reflect adsorbate (e.g., adsorbed O(H) and H) species on the catalyst surface. Prior to the advent of the $\Delta\mu$ technique, these interactions ($O(H)_{ads}$ and H_2O_{ads}) were only observable in small cluster sizes, as noted above, due to their weak scattering and nonspecific adsorption on the electrocatalyst surface. This technique has been successfully applied to Pt and Pt-M electrocatalysts to study a variety of adsorbates under in situ conditions.[2,28−32]

The water activation pathway is of particular interest in elucidating the mechanisms for the ORR on an electrocatalyst surface. Adsorbed OH serves as a surface poison on Pt electrocatalysts by effectively blocking the active sites for molecular O adsorption.[2] Evidence of this effect has been gathered from both spectroscopic and electrochemical investigations.[28,33] Further, a recent body of work used density-functional theory in conjunction with experimental data to model various oxo-species as they relate to ORR and the apparent activation energies on Pt and Pt-alloys. These studies assisted in further elucidating the effects of alloyed transition metals in Pt electrocatalysts.[34,35] These alloyed metals were found to increase the activity of the electrocatalysts by either (a) taking the brunt of the OH adsorption and because of OH−OH repulsions leaving the Pt sites more free to proceed with ORR, or (b) partially deactivating the Pt surface (hence, increasing the partial valence of Pt), which shifts the onset of OH adsorption to higher potentials.[2,33,36]

Incorporating the information gathered from these previous studies on Pt-based electrocatalysts, we recently published the first ever communications regarding the spectroscopic observation of the water activation process on a chalcogenide electrocatalyst (30 wt % Rh_xS_y/C, commercially available from De Nora).[3,37] This material is the current state-of-the-art chalcogenide-based electrocatalyst, available as an oxygen depolarized cathode (ODC).[38] Recent reports provide insight into the inherent stability of this material in HCl-saturated ORR environments.[13,39] The De Nora Rh_xS_y/C electrocatalyst exhibits the highest ORR performance and stability of the sulfide-based chalcogenide electrocatalysts.[4] Further, this electrocatalyst does not contain selenium, which owing to its toxicity, likely will cause the higher-performing Ru_xSe_y-class of chalcogenide electrocatalysts[6,40] to be ruled untenable for consumer applications. The performance and structural characteristics of the Rh_xS_y/C electrocatalyst renders it an ideal model compound for investigation of the ORR pathway on a sulfur-based chalcogenide electrocatalysts.

Despite its high level of performance, it is unlikely that Rh_xS_y/C will ever be a viable alternative to Pt-based electrocatalysts in PEMFC or DMFC applications. While Pt is expensive, Rh is typically 5−10 times more costly.[41] In addition, Rh does not exhibit the high degree of methanol tolerance of Ru-based chalcogenide electrocatalysts.[42] Nevertheless, the Rh_xS_y/C electrocatalyst is well-accepted for applications in chlorine generation.[13] Here the traditional hydrogen evolution cathode is replaced with an oxygen reduction analog, thereby providing a 800−900 mV reduction in cell voltage and saving an equivalent of 700 kWh ton^{-1} of chlorine.[43,44]

The De Nora Rh_xS_y/C electrocatalyst is comprised of a balanced phase of Rh_2S_3, Rh_3S_4, and $Rh_{17}S_{15}$.[45−47] XRD studies of the commercially produced material only reveal a spectrum for the $Rh_{17}S_{15}$ phase. The lack of observable XRD patterns for the Rh_2S_3 and Rh_3S_4 phases does not indicate their absence but rather that they exist as extremely small particles (small grain sizes) in comparison to the $Rh_{17}S_{15}$ phase. Thus, the microcharacterization of this material by standard methods (e.g., XRD) is severely limited by the uncertainty regarding the fraction of these phases and their complex structure. In a prior communication, application of the $\Delta\mu$ technique to in situ XAS water activation studies in 1 M trifluoromethanesulfonic acid (TFMSA) coupled with laboratory rotating disk electrode experiments suggested that the active phase in the Rh_xS_y/C electrocatalyst is Rh_3S_4.[3]

That initial work was conducted solely on the mixed-phase Rh_xS_y/C electrocatalyst, as the constituent phases were not available in any substantial quantity with sufficient purity. Here, we present water activation and ORR studies on thermally grown carbon-supported Rh_2S_3 and Rh_3S_4 preferential phases in 1 M TFMSA. In addition, the Rh_xS_y/C catalyst was further probed in 6 M TFMSA electrolyte (i.e., water content is significantly lower).[33,48] These additional studies confirm the initial conclusions that Rh_3S_4 is the more active phase,[3,37] but also point out the instability of the Rh_xS_y catalyst in strong acid such as TFMSA. Further, high acid concentrations result in the formation of a Rh skin on the electrocatalyst particle surfaces, and this may in fact be the more active constituent. These results also serve to fully validate the $\Delta\mu$ technique as a powerful new tool for elucidating the active sites of mixed-phase inorganic complexes for ORR electrocatalysts. To the authors' knowledge, this is the first time the active site has been determined in a complex mixed inorganic complex to this high level of detail. Therefore, the present work constitutes a major advance in our understanding of electrocatalysis on systems very different from the conventional metal cluster surfaces. This work is expected to open new avenues for materials synthesis tailored for particular applications.

2. Experimental Section

2.1. Synthesis. Rh_xS_y/C (30 wt %; De Nora) and 30 wt % Rh/C (8.3 nm grain size, E-TEK, Inc., now "BASF Fuel Cell, Inc.", Somerset, NJ) were used in as-received form. The carbon support was Vulcan XC-72 (Cabot Corporation). The properties and morphology of the 30 wt % Rh/C electrocatalyst (i.e., 8.3 nm grain size) were reported in a prior publication.[13] The synthetic methodology for the Rh_xS_y/C electrocatalyst can be found in the patent literature.[49−51] The preferential phases, 40−45 wt % Rh_2S_3/C (orthorhombic *Pbcn*)[47] and Rh_3S_4/C (monoclinic, space group *C*2/*m*),[45] were prepared by heat treating the carbon-supported 30 wt % Rh_xS_y precursor material (De Nora) under conditions outlined by Beck et al.[45] Briefly, this involved heating the samples under flowing argon (high purity, Medtech Gases, Inc.) in a quartz furnace tube for ≈2 h at 1220 and 1340 K for Rh_2S_3 and Rh_3S_4, respectively. Attempts to generate a preferential $Rh_{17}S_{15}$ phase from the precursor were unsuccessful and resulted in a near complete breakdown of the Rh−S precursor into metallic Rh.

2.2. Catalyst Morphology (XRD and High-Resolution Transmission Electron Microscopy). XRD data were obtained with high-resolution synchrotron radiation at beamline X-7B at the National Synchrotron Light Source (NSLS, Brookhaven National Laboratory, Upton, NY). The as-synthesized catalyst powders were packed into amorphous glass capillaries. The X-ray radiation, adjusted to a wavelength of 0.9177 Å via a Si(111) monochromator, was chosen as to prevent XAS signals from interfering with the XRD spectra. Data was acquired through a MAR345 image plate detector (marUSA, Evanston, IL). Owing to the high intensity of the X-ray beam (flux $\approx 6 \times 10^{11}$ photons sec^{-1}) it required less than 15 min per sample to collect a full XRD pattern.

All three of the as-synthesized samples were examined using a 300 kV FEI Tecnai F30 ST field-emission gun high-resolution transmission electron microscope. This instrument is equipped with a lithium-drifted silicon detector for X-ray energy dispersive spectrometry (XEDS). Specimens for high-resolution transmission electron microscopy (HRTEM) were prepared by dispersing each nanoscale electrocatalyst in methanol and ultrasonicating them (10 min) to reduce agglomeration. Subsequently, a single drop of each dispersion was deposited onto either a thin carbon film supported by a copper grid or a carbon film was dipped into the dispersion.

2.3. Rotating Disk Electrode Studies. Rotating disk electrode (RDE) studies were conducted in $O_{2(g)}$-saturated (MedTech Gases, Inc.) 1 M TFMSA (3 M Corporation). The as-received TFMSA electrolyte was distilled and purified prior to use.[48,52] TFMSA was chosen as the supporting electrolyte because of its low anion adsorption.[31] The RDE setup was comprised of a glassy carbon (GC) RDE (5.6 mm diameter, Pine Instrument Co.) interfaced with a model AFASR rotator (Pine). Potentiostatic control (for both the RDE and in situ XAS studies) was obtained with a model PGSTAT30 potentiostat/galvanostat (Eco Chemie, Brinkmann Instruments). Prior to all RDE experiments, the GC was polished to a mirror-finish with 1 and 0.05 μm alumina slurry (Buehler, Inc.). The inks were comprised of a mixture of the relevant electrocatalyst and a small amount of 5 wt % Nafion as a binder (Sigma-Aldrich). The suspension was a 1:1 wt % mixture of 2-propanol (HPLC grade, Sigma-Aldrich) and deionized water (MegaPure, Millipore). The target geometric loading of the cast electrocatalyst films on the GC were 14 μg metal cm^{-2}. The final metal/Nafion mass ratio in the dried film was <1:50 and thus allowed for additional diffusion effects when analyzing the RDE data to be neglected.[33,53] This procedure emanates from long experience of our in-house RDE measurements.[3,4,33] As a part of this protocol, statistical tests using in-house ICP-MS measurements are made to ensure the metal loading of the deposits to be within a range of ±2%.

For all electrochemical experiments (RDE and in situ XAS), a Pt mesh (Alfa Aesar) served as the counterelectrode with a sealed RHE as the reference electrode. The RHE was generated from the identical electrolyte to eliminate the possibility of junction potentials. All potentials are reported relative to RHE. The catalysts were activated (under $Ar_{(g)}$-purged conditions) prior to RDE studies by collecting cyclic voltammograms at 50 mV s^{-1} until a steady state signal was achieved (typically 30 cycles). RDE data was obtained in room temperature electrolyte at 100, 400, 625, 900, 1225, and 1600 rpm (rotations per minute).[3,4,13] Data were collected at each rotation rate for five scans (20 mV s^{-1}), and the final three scans were averaged for analysis. To ensure reproducibility, each data set was collected at least three times with separately cast RDE films. All electrochemical analysis[54] was performed on the cathodic sweeps.

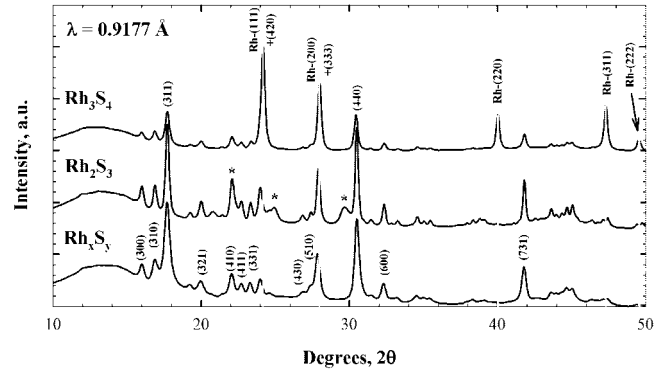

Figure 1. Capillary powder X-ray diffractograms for the Rh−S electrocatalysts from high-resolution (0.9177 Å) synchrotron radiation (NSLS beamline X-7B) studies. The Rh_xS_y diffractogram is indexed to Pm3m $Rh_{17}S_{15}$. The gray vertical lines denote the expected pattern for cubic Fm3m elemental rhodium. The asterisks denote possible reflections from the *Pbcn* Rh_2S_3 phase.

2.4. XAS Data Collection and Analysis. Details on the experimental equipment and materials have been published recently.[3,4,37] One important difference in this report involves the utilization of 6 M TFMSA. To study the effect of water activity with the Rh_xS_y/C material, concentrated solid 9 M monohydrate was diluted to 6 M. Special care was taken with the distillation and crystallization of the TFMSA in accordance with previously reported procedures.[33,48,52] To ensure that the total water content was kept as low as possible, both of the electrodes as well as the Nafion 112 separator were soaked in deaerated 6 M TFMSA for 2 h prior to cell assembly.

Following an activation step (0.02 to 1.2 V vs RHE at 20 mV s^{-1}), full Rh K edge (23220 eV) EXAFS scans (−250 eV to 16 k) were collected at different potentials by cycling the cell to the respective anodic potential and holding potentiostatically during the absorption measurements (representative cyclic voltammograms of the electrocatalysts is available in the Supporting Information section). All XAS signals were collected with a beam spot size of 0.3 × 1.5 mm. These measurements were collected in fluorescence mode via a 13-element fluorescence detector at beamline X18-B (National Synchrotron Light Source, Brookhaven National Laboratories, Upton, NY). During all the measurements, transmission data were collected in conjunction with a thin Rh foil to account for shifts in measured energy due to drifts in the Si(111) monochromator position. For alignment, background subtraction, and normalization of the XAS data, the IFEFFIT suite[55] was utilized.

The theory and normalization processes for the $\Delta\mu$ analysis are described in detail elsewhere.[3] Briefly, the collected spectra were aligned by using the signals from the reference foil in order to preserve any shifts in the absorption edge arising from oxidation of the Rh. The aligned spectra were then carefully normalized in a previously described manner.[27,28] It should be noted that the normalization range appropriate for $\Delta\mu$ analysis is significantly more constrained than for typical EXAFS analysis. In order to isolate the adsorbate scattering, the normalization was applied in the range 40−200 eV past the edge.

The $\Delta\mu$ signals were generated according to the relationship

$$\Delta\mu = \mu(\mathrm{V}) - \mu(0.40\ \mathrm{V}) \quad (1)$$

Where, the signal at 0.40 V is considered the cleanest (e.g., double layer) region free of adsorbed H, O(H), and anions as

TABLE 1: Crystallography[a]

	symmetry	space group	cell parameters						Rh−Rh_{avg}, Å	Rh−S_{avg}, Å
			a/Å	*b*/Å	*c*/Å	α/°	*β*/°	*γ*/°		
Rh	cubic	Fm3m	3.803			90			2.69	
Rh_2S_3	ortho- rhombic	*Pbcn*	8.462	5.985	6.138	90			3.208	2.365
Rh_3S_4	monoclinic	*C*2/*m*	10.292	10.671	6.213	90	107.71	90	2.70/ 3.092	2.30
$Rh_{17}S_{15}$	cubic	Pm3m	9.911			90			2.59	2.33

[a] References: Rh (JCPDF #01-1214), Rh_2S_3 (ref 47), Rh_3S_4 (ref 45), $Rh_{17}S_{15}$ (JCPDF #73-1443, ref 47).

determined via the electrochemical analysis and EXAFS fitting. All potentials correspond to a point on the anodic sweep. For signals at 0.50 and 0.60 V, a correction to account for both charging effects of the electrode and the Rh lifetime core width was performed.[27,56] Interpretation of the acquired spectra was accomplished by generating XANES spectra via the FEFF 8.0 code[57] utilizing models of the pertinent Rh−S clusters generated with CAChe (version 6.1.12, Fujitsu Computer Systems Corporation) from published[45−47] and experimental[3,13,39] crystallographic parameters. The theoretical spectra were then treated to the same subtraction process as the experimental results: $\Delta\mu = \mu(Rh_xS_y\text{-}O_{ads}) - \mu(Rh_xS_y)$.

3. Results and Discussion

3.1. Morphology. ***3.1.1. X-ray Diffraction.*** Figure 1 presents the high resolution synchrotron ($\lambda = 0.9177$ Å) powder X-ray powder diffraction results for the carbon-supported rhodium sulfide electrocatalysts. As discussed in prior publications,[3,13] the XRD spectrum for the Rh_xS_y/C electrocatalyst is very complex. It is well established[45] that this system is composed of a balanced phase mixture of cubic Pm3m $Rh_{17}S_{15}$,[46] orthorhombic *Pbcn* Rh_2S_3,[47] and monoclinic *C*2/*m* Rh_3S_4[45] (Table 1). Nonetheless, only the $Rh_{17}S_{15}$ phase could be accurately indexed to the Rh_xS_y/C spectrum. This suggests that the grain size of the $Rh_{17}S_{15}$ is much larger than that of the other Rh−S phases, thereby limiting the utility of XRD for determination of the phase balance.

Utilizing the derived values reported by Beck et al.,[45] the carbon-supported Rh_xS_y precursor was heat-treated at 1220 K in an effort to skew the phase balance toward the Rh_2S_3 phase. The resulting XRD pattern (Figure 1, middle) is again dominated by the fingerprint of the $Rh_{17}S_{15}$ phase, although very small elemental Rh metal (Fm3m) could also be present. Despite the complexity of the X-ray diffractogram, several features (marked by asterisks) suggest that the thermal growth of Rh_2S_3 was successful. The peak at 22.1° could be representative of combined (311) and (212) reflections[47] from nanoscale Rh_2S_3 particles overlaid with the (410) reflection[46] of $Rh_{17}S_{15}$. If this is the case, then the peak at 24.9° can be considered the (022) and (400) reflections from Rh_2S_3. It is important to note that these reflections seen at 22.1 and 24.9° give the second and third most intense reflections for Rh_2S_3. Further evidence for the presence of nanocrystallites of Rh_2S_3 can be seen at 29.7 and 30.5°. Indexing the peak at 29.7° to the (213) reflection of Rh_2S_3 provides for an elegant explanation for the larger magnitude of the $Rh_{17}S_{15}$ (440) peak compared to the $Rh_{17}S_{15}$ (333) reflection in the Rh_2S_3 spectrum versus the Rh_xS_y spectrum. At 30.5° the Rh_2S_3 should exhibit a high intensity peak composed of combined reflections from the (402), (231), and (420) facets. In combination with the (440) reflection from the omnipresent $Rh_{17}S_{15}$ phase, this peak should appear with greater intensity than in the Rh_xS_y spectrum.

In contrast to the other Rh−S spectra, the XRD pattern for the Rh_3S_4 preferential phase (Figure 1, top) exhibits a strong fingerprint from elemental Rh. These features are so dominant that the $Rh_{17}S_{15}$ reflections are quite muted with respect to the other Rh−S XRD spectra. The Rh_3S_4 preferential phase spectrum could not be indexed to either Rh_3S_4 or Rh_2S_3. Thus, if the Rh_3S_4 phase is present in this material, it is nominally crystalline in comparison to the $Rh_{17}S_{15}$ phase and is therefore invisible to the powder XRD technique.

3.1.2. Transmission Electron Microscopy. XEDS confirmed that all three of the as-synthesized samples were composed of only carbon, rhodium, and sulfur. A montage of several typical TEM images of the three samples is presented in Figure 2. Figure 2a−c are low-magnification bright-field TEM images showing the size distribution of the particles for samples Rh_xS_y, Rh_2S_3, and Rh_3S_4, respectively. The catalyst particles generally had diameters of less than 20 nm, though it could vary significantly. The globular amorphous carbon support is omnipresent and generally interferes with TEM imaging and analysis. The larger darker particles (with diameters 10−25 nm in the Rh_2S_3 and up to 100 nm in the Rh_3S_4 samples) suggest the growth of Rh metal particles with heating to higher temperatures, which is in good agreement with the XRD data.

Figure 2d−h are HRTEM images of the corresponding as-synthesized nanoparticles. The speckle pattern in the background of the images originates from the continuous amorphous carbon support film. The bright and dark contours around the edges of the particles, especially visible in images (d) and (g), are Frensel fringes, which are imaging artifacts caused by aberrations of the electron optics that appear when defocusing the objective lens as required to generate phase contrast. The catalyst nanoparticles of each of the three samples were found to form intimate contacts with the globular amorphous carbon support. Interestingly, it is sometimes found (e.g., Figure 2g) that these particles actually wet their amorphous carbon support (i.e., make a contact angle <90°).

Figure 2d was recorded from the Rh_xS_y sample and shows several agglomerated catalyst particles. The crystal structure of the most distinct one seems to belong to the cubic system. The lattice planes apparent in the HRTEM image originate from {410} planes oriented along the directions from the top right to the bottom left, and from the top left to the bottom right, respectively.

Figure 2e,f was recorded from the Rh_2S_3 sample and illustrate the morphology of two different catalyst particles with diameters ≈12 and ≈25 nm, respectively. These particles exhibit faceting on crystallographic planes of a much greater extent than observed in Figure 2d,g. The Rh_3S_4 sample notably contained only small Rh−S phase particles with diameters of only a few nanometers (Figure 2g) in addition to the large Rh particles. The HRTEM image of Figure 2h shows a portion of a larger nanoparticle from the Rh_3S_4 sample. Likely, this particle is Pm3m $Rh_{17}S_{15}$ viewed in a <521> or a <311> direction (which generate very similar fringe patterns). In this case, the dominant lattice fringes correspond to {311} or {310} planes.

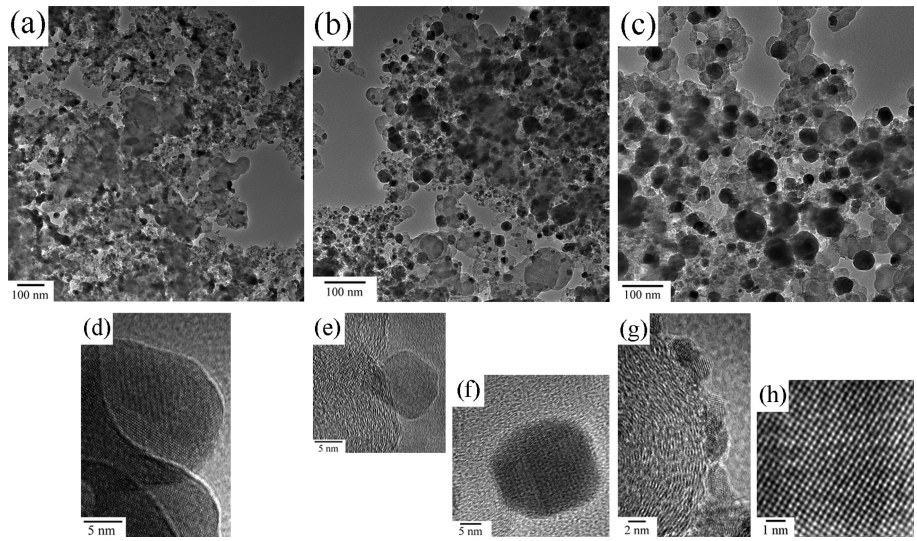

Figure 2. TEM images of Rh−S electrocatalysts. (a−c) Low magnification bright-field TEM images obtained from samples Rh_xS_y, Rh_2S_3, and Rh_3S_4, respectively. (d) A nanoparticle from the Rh_xS_y sample in contact with several others. (e, f) Two images of nanoparticles recorded from sample Rh_2S_3 in intimate contact with the amorphous globular carbon support. (g) Nanoparticles of the Rh_3S_4 sample, wetting the surface of the amorphous globular carbon support. (h) HRTEM image of a nanoparticle of the Rh_3S_4 sample, viewed in either the <521> or a <311> direction.

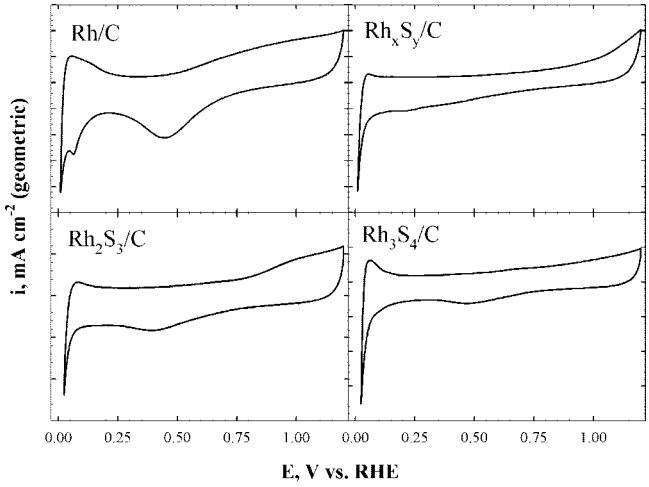

Figure 3. Room temperature 50 mV s^{-1} cyclic voltammograms of the denoted catalysts in deaerated 1 M TFMSA.

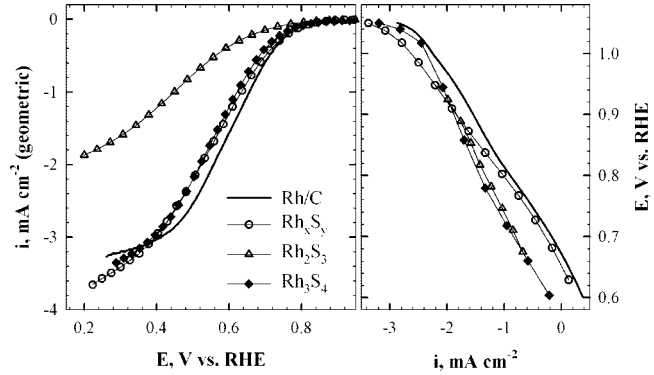

Figure 4. RDE (900 rpm) results for the standard 30 wt % Rh/C, 30 wt % Rh_xS_y/C (De Nora), and the thermally grown Rh_2S_3/C and Rh_3S_4/C preferential phases. Cathodic scans in room temperature O_2-saturated 1 M TFMSA, 20 mV s^{-1} scan rate.

3.2. Electrochemical Kinetics. ***3.2.1. Cyclic Voltammetry.*** Figure 3 shows 50 mV s^{-1} cyclic voltammograms of the four electrocatalysts in $Ar_{(g)}$-purged 1 M TFMSA. The standard 30 wt % Rh/C electrocatalyst (Figure 3, top left) exhibits features correlated to the adsorption/desorption of H and oxo-species.[58,59] The large cathodic peak centered at ≈0.48 V can be assigned to the reduction of adsorbed oxo-species on the rhodium surface. At potentials <0.25 V, hydrogen adsorption/desorption features are apparent, and evidence of hydrogen evolution is observed at the lowest anodic potential (0.02 V). On the anodic sweep, a smooth double layer region is observed just past the hydrogen desorption region at ≈0.25−0.45 V. Immediately following this a gradual increase in the anodic current begins. This is attributed to oxo-species adsorption on the electrocatalyst surface beginning with water activation. If the scan was continued to potentials greater than 1.25 V, it is expected that the onset of oxygen evolution would become apparent.

In contrast, the CV for Rh_xS_y/C is considerably muted. This material does not possess the broad cathodic feature seen with Rh/C, although a small peak is observable at ≈0.24 V. Further, while a hydrogen evolution peak is discernible, the catalyst does not exhibit a significant H_{des} peak. Finally, the broad increase in the anodic current typically assigned to the progression of $OH/(H_2O) \rightarrow O_{ads}$ on Rh/C is arguably nonexistent until ≈0.90 V, whereas this feature becomes noticeable on the standard Rh/C electrocatalyst a full ≈450 mV earlier.

When compared to the Rh/C and Rh_xS_y/C electrocatalysts, the Rh_2S_3/C and Rh_3S_4/C preferential phases exhibit a mixture of features. For Rh_2S_3, the depth of the cathodic feature is still small, but has shifted to a higher potential in comparison to the Rh_xS_y/C electrocatalyst. Further, the Rh_2S_3 preferential phase exhibits a noticeable increase in anodic current at 0.75 V. The magnitudes of the cathodic and anodic features of the Rh_3S_4 preferential phase sit between the Rh_xS_y/C and Rh_2S_3/C electrocatalysts. Further, the CV for the Rh_3S_4 phase is differentiated by the well-defined (and considerably larger) H_{des} peak, as opposed to Rh_2S_3/C; this however is still considerably smaller in magnitude compared to the corresponding peak in the case of Rh/C. Despite this similarity with Rh/C, the Rh_3S_4 preferential phase is comparably devoid of the anodic oxo-species adsorption features exhibited by Rh/C.

These CV curves will be more carefully correlated with the $\Delta\mu$ results and interpreted below.

TABLE 2: Electrochemical Kinetics[a]

catalyst	E_{onset}[b], V vs RHE	$-b$, mV dec^{-1}	i at 0.9/0.8/0.7 V[c], 10^3 mA cm^{-2}	i_k at 0.85 V[b], 10^3 mA cm^{-2}
Rh	1.05	140	21.4 94.5 591	58
Rh_xS_y	1.05	124	16.1 103 507	36
Rh_2S_3	0.93	190	14.4 45.0 150	26
Rh_3S_4	1.05	196	24.8 90.6 404	29

[a] Room temperature 1 M TFMSA, 900 rpm, 20 mV s^{-1} scan rate. [b] Determined by 1st derivative analysis of the cathodic ORR sweep. [c] Geometric area.

3.2.2. RDE Studies. The performance of the electrocatalysts in $O_{2(g)}$-saturated 1 M TFMSA was determined via the RDE technique (Figure 4). The electrocatalysts reveal a single reduction wave suggesting single reaction sites. In terms of gross current density and ORR onset potential (Table 2), the Rh_2S_3 preferential phase significantly lags behind the other electrocatalysts. Unlike Rh/C, the Rh−S electrocatalysts do not exhibit clear, well-defined limiting currents. This property was previously reported for the Rh_xS_y/C electrocatalyst,[3,4] and the limiting currents were therefore approximated by utilizing the potential where the slope of the ORR curve became constant (≈0.30 V determined by a first derivative analysis). Further, the Rh−S phases do not possess an H_{des} region that would allow for proper determination of the electrochemical surface areas.[53] As a result, all current densities (also for Rh/C) are reported with respect to the mass-normalized (14 μg total Rh) geometric surface areas.

Approximation of the limiting currents allowed for extraction of the mass transfer-corrected Tafel slopes (Figure 4, right) and relevant kinetic parameters (Table 2). Both Rh/C and Rh_xS_y/C exhibit Tafel slopes of ≈120 mV dec^{-1} in the kinetic/diffusion-controlled region, and a lower slope of ≈60 mV dec^{-1} at very low overpotential. The well-established interpretation for these values is that the −120 mV dec^{-1} slope is indicative of 4e$^-$ electron transfer whereas the lower slope can be attributed to oxo-species adsorption on an oxide-covered surface.[33,60−62] These results indicate that both Rh/C and Rh_xS_y/C effectively accomplish ORR via a kinetic pathway similar to Pt/C. In particular, these results bolster the determined apparent activation energies for Rh_xS_y/C in prior publications,[3,4] which were found to trend downward with respect to increasing overpotential. An identical trend has been reported for Pt and Pt-alloy electrocatalysts.[33] Subsequent experimental and theoretical studies[35] have shown that the pre-exponential factor is influenced by the surface oxide/oxo-species coverage. Considering the similarity of Rh_xS_y/C to the results reported for Pt and Pt-alloy electrocatalysts, it is reasonable to expect that the water activation and ORR processes on Rh_xS_y/C proceed similarly to that on the active sites of Pt.

In contrast to Rh/C and Rh_xS_y/C, the preferential phases show significantly higher Tafel slopes of ≈190 mV dec^{-1}. This trend could be indicative of a larger cathodic transfer coefficient for the preferential phases, differences in diffusion at the electrocatalyst surfaces, an increase in the number of active sites with decreasing potential, or just a larger resistance in these preferential phases. A proper determination of these parameters would require true, single phases, but such materials were unavailable for this study. Indeed, the aforementioned XRD and HRTEM analyses show that the preferential phases still contain a substantial number of large $Rh_{17}S_{15}$ particles, and increasing amounts of elemental Rh metal with heating. Considering the nanocrystalline nature (i.e., high surface areas) of the Rh_2S_3 and Rh_3S_4 particles, however, the majority of the exhibited activity of the preferential phases can be attributed to the target phases. While it was not unexpected that the Rh_3S_4 preferential phase would show ORR activity, the results for the Rh_2S_3 preferential phase are somewhat surprising and will be explained below.

3.3. XAS Analysis. ***3.3.1. In Situ XANES.*** Figure 5 presents normalized in situ (0.40 V) Rh K edge (23220 eV) absorption spectra for the Rh−S electrocatalysts in addition to the standard 30 wt % Rh/C. The Rh/C electrocatalyst exhibits the signature of Rh metal in the oscillatory features. The nanoscale nature of the Rh particles is reflected in the low magnitudes of these oscillations. In contrast to the metallic Rh/C spectrum, the Rh_xS_y/C signal possesses a more intense white line at 5−50 eV past the edge. The white line in an XAS μ(E) spectrum is attributed to excitation into the electron vacancies in the d-type valence orbital.[24,63,64] Typically, this feature will grow as the extent of ligation around the absorbing atom increases thus increasing the electron vacancy. As expected, the Rh_xS_y/C electrocatalyst (consisting of sulfided Rh species) exhibits a substantial increase in this feature compared to the Rh/C electrocatalyst. With heating to higher temperature to prepare the Rh_2S_3 and Rh_3S_4 preferential phases, the spectra increasingly revert back to the Rh/C signature reflecting the Rh particles being formed as indicated above by the XRD and TEM data.

3.3.2. In Situ Rh K edge EXAFS. Figure 6 presents the χ(k) (k^2-weighted) spectra derived from spectra similar to that in Figure 5. With the exception of the Rh_2S_3 preferential phase, the materials exhibit oscillations to 14 k reflecting the quality of the collected data. These spectra again reveal the transformation of the Rh_xS_y spectrum to that more resembling the Rh/C spectrum with heating to higher temperature to form the preferential phases.

The nonphase-corrected Fourier transforms (FT) of these data are presented in Figure 7. These FT spectra reflect the interatomic distance (in units of Å, ± 0.02 Å) between the absorbing Rh atom and its neighbors, either S or another Rh atom with the intensity reflecting the product of the coordination number (N_{Rh-X}) and Debye−Waller factor (σ^2).[63] The Rh/C standard exhibits a large peak at the expected position for Rh−Rh (average R_{Rh-Rh} = 2.69 Å) interactions in Rh. The Rh_x-S_y electrocatalysts all show features at lower R that are attributed to Rh−S interactions. Note that the ratio of intensities I_{Rh-Rh}/I_{Rh-S} increases in the order xy < 23 < 34, reflecting the

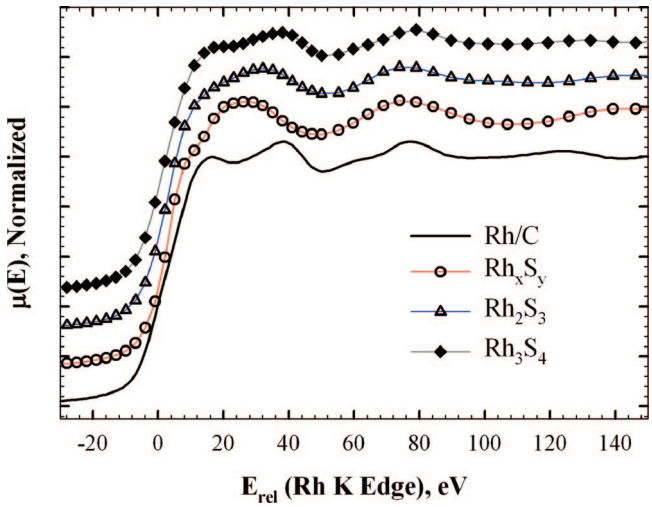

Figure 5. In situ (0.40 V) Rh K edge (23220 eV) XANES signals for the electrocatalysts in deaerated 1 M TFMSA.

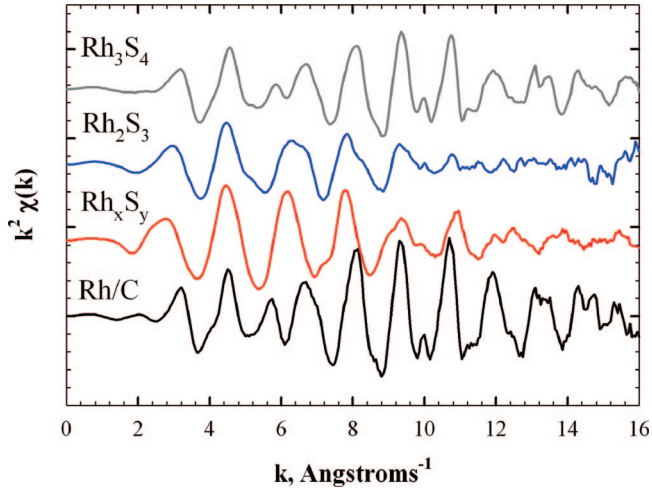

Figure 6. In situ (0.40 V) Rh K edge (23220 eV) k^2-weighted χ(k) spectra for the electrocatalysts in deaerated 1 M TFMSA.

formation of Rh particles with heating during the preparation of the preferential phases as evident already in the XANES and raw EXAFS data discussed above. As outlined in Table 1, Rh_2S_3 is an orthorhombic (ABAB stacking) crystal with the space group *Pbcn* and is essentially comprised of canted rows of RhS_6 clusters. As shown in the model of Figure 8, it does not possess direct Rh−Rh bonds, yet Figure 7 clearly shows an Rh−Rh peak (albeit small) reflecting the some Rh particle formation from heating.

A representation of the monoclinic *C*2/*m* Rh_3S_4 cluster is shown in the top right of Figure 8. It is in this view that the intimate interrelationship of the Rh−S phases becomes apparent. Indeed, the RhS_6 clusters that fully comprise the Rh_2S_3 crystal, are present as a sulfur-rich backbone in the Rh_3S_4 phase. To either side of the Rh_2S_3 backbone in the Rh_3S_4 material are canted metallic Rh_6 "octahedra". Thus, the extent of Rh−Rh bonding is much higher in this component than in the Rh_2S_3 backbone. However, the magnitude of the Rh−Rh peak is much larger than expected for a pure Rh_3S_4 sample, and it too reflects the large Rh clusters existing in this sample. The primitive cubic $Rh_{17}S_{15}$ (Pm3m) system is shown at the bottom right of Figure 8. This phase is comprised of two unique Rh−S domains: a series of RhS_4 "chains" and heavily sulfided cubes of Rh_8. While $Rh_{17}S_{15}$ has been reported to act like a superconductor,[46,65] its

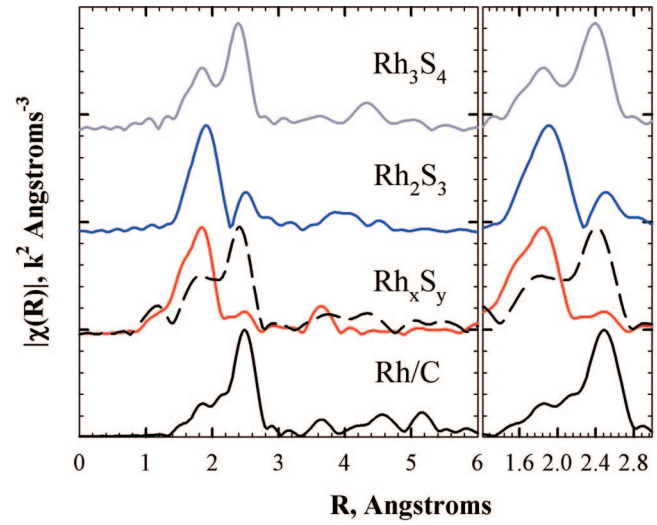

Figure 7. In situ (0.40 V), nonphase-corrected, Rh K edge (23220 eV) k^2-weighted $|\chi(R)|$ spectra for the electrocatalysts in deaerated 1 M TFMSA. The spectrum for Rh_xS_y at 0.40 V in deaerated 6 M TFMSA is represented by the overlaid dashed line on the 1 M spectrum.

metallic character is considerably lacking, no doubt in part due to the magnitude of Rh−S interactions. Finally, a representation of face centered cubic Rh (Fm3m) is given at the bottom right of Figure 8, with an Rh_6 Janin-type[66] cluster showing fcc and hcp adsorption sites.[27,67]

The XRD (Rh metal peaks), TEM (visible black clusters), XANES (spectral signature), and EXAFS (Rh−Rh peaks in FT) data all show that the Rh_xS_y sample undergoes Rh metal particle growth with respect to increasing temperature, so that the Rh particle size increases in the order: Rh_xS_y < Rh_2S_3 < Rh_3S_4. This explains the Rh−Rh peak in the FT-EXAFS for the Rh_2S_3 (Rh−Rh distances do not exist in the pure crystalline Rh_2S_3 phase), and the very large Rh−Rh peak for in Rh_3S_4 (much larger than expected from the inherent Rh−Rh "coordination" in the pure Rh_3S_4 phase). Nevertheless, it is instructive to fit the Rh−Rh and Rh−S peaks and Figure 9 presents a graphical representation of the high quality of these fits obtained on Rh_3S_4 at 0.4 V (referred to as the "clean potential region") showing the fit of the Rh K edge Fourier transform of the sample fit to the two shell Rh−S and Rh−Rh interactions. Tables 3−5 present the fitting results over the entirety of the experimental electrochemical range for Rh_2S_3, Rh_3S_4, and Rh/C, respectively, and Figure 10 plots the change in N_{Rh-Rh} ($\delta N = N(x\ V) - N(0.3\ V)$) for the Rh_3S_4 and Rh/C catalysts.

The results for both the Rh_3S_4 and Rh/C catalysts in Figure 10 show a similar trend, an initial decrease, followed by an increase, and then a final decrease. This strongly suggests that both results reflect the behavior of metallic particles, and hence that the EXAFS results for the Rh_3S_4 sample are dominated by the comparably large 100 nm Rh particles seen in the HRTEM and not that from the RhS phases. The initial decrease is due to water desorption (which we will confirm from the $\Delta\mu$ data below). In the absence of adsorbates, we have noted many times previously that metallic particles (such as Pt and Ru) tend to flatten out to increase their interaction with the support and thereby decrease the average N_{Rh-Rh}. Upon adsorption of atop OH, the Rh particles again become more round and the N_{Rh-Rh} again increases. The final decrease is due to atop OH moving to 3-fold O (with loss of H) and even subsurface O, which decreases the Rh−Rh scattering. We have seen the exact same trend with Pt many times previously.[2,28,31,32] The shift to higher potentials for the Rh_3S_4 sample suggests that the large 100 nm

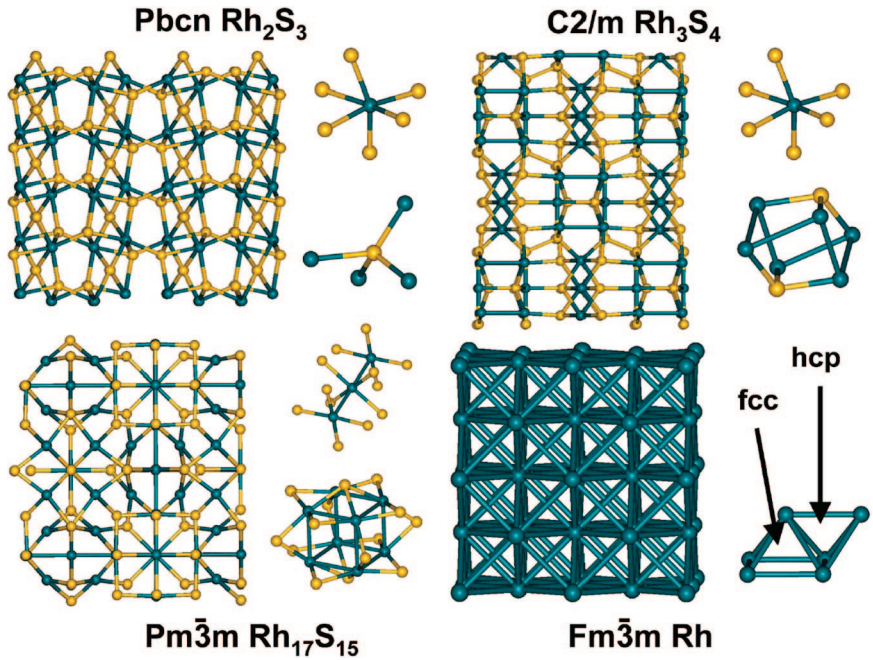

Figure 8. Three dimensional representations of the Rh−S phases and Rh metal: Rh (dark), sulfur (yellow). Clusters: (top left) Rh_2S_3, RhS_6, and Rh_4S, (top right) Rh_3S_4, RhS_6, and Rh_6S_2, (bottom right) Rh, Rh_6 Janin cluster, (bottom left) $Rh_{17}S_{15}$, RhS_4 chains, sulfided Rh_8 cube.

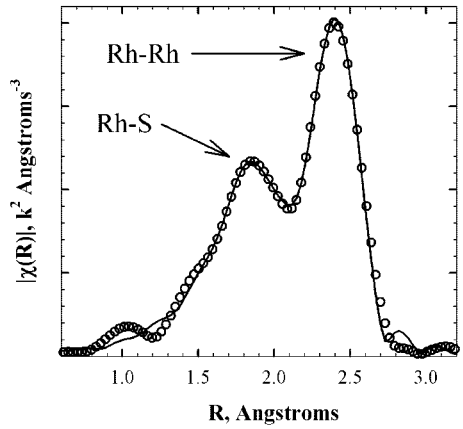

Figure 9. Comparison of the nonphase-corrected k^2-weighted Fourier transform data for the Rh_3S_4/C preferential phase at 0.40 V in deaerated 1 M TFMSA (○) and a two-shell (Rh−S and Rh−Rh) fit (−).

TABLE 3: First Shell EXAFS Fit Results for Rh_2S_3/C[a]

E, V vs RHE	N_{Rh-S}[b]	R_{Rh-S}[b], Å	E_0, eV
0.30	2.52	2.320	−0.397
0.40	2.51	2.323	7.231
0.50	2.43	2.316	4.295
0.60	2.57	2.319	1.999
0.70	2.43	2.320	5.935
0.80	2.20	2.319	3.499
0.90	2.28	2.314	6.565
1.00	2.32	2.316	3.334

[a] S_0^2 fixed at 0.921 as calculated via FEFF8.0, k range: 2.5−15.5 Å^{-1} (k^2), R range: 1.8−3.3 Å. Gross errors: $N \pm 20\%$, $R \pm 0.02$ Å. [b] σ^2 fixed at 0.004 Å^2 from ref 47.

Rh particles in this case are much less reactive than the smaller particles in the Rh/C sample; the peak maximum due O(H)/O_{sub} adsorption shifted from 0.65 to 0.9 V. This 250 mV shift on Rh is similar to a nearly 350 mV shift with Pt when going from small Pt particles to single crystal Pt(111).[68,69]

TABLE 4: First Shell EXAFS Fit Results for Rh_3S_4/C[a]

E, V vs RHE	N_{Rh-Rh}[b]	R_{Rh-Rh}[b], Å	E_0, eV	N_{Rh-S}[c]	R_{Rh-S}[c], Å	E_0, eV
0.30	3.63	2.687	−1.642	1.82	2.331	−4.368
0.40	3.66	2.683	8.316	1.78	2.318	6.492
0.50	3.48	2.690	1.254	1.84	2.310	−1.305
0.60	3.64	2.686	2.114	1.85	2.318	0.683
0.70	3.45	2.690	1.415	1.81	2.307	−1.443
0.80	3.50	2.686	5.254	1.79	2.311	3.921
0.90	3.60	2.692	3.403	1.69	2.306	0.560
1.00	3.29	2.680	0.654	1.82	2.321	2.087

[a] S_0^2 fixed at 0.921 as calculated via FEFF8.0, k range: 2.5−15 Å^{-1} (k^2), R range: 1.8−3.4 Å. Gross errors: $N \pm 20\%$, $R \pm 0.02$ Å. [b] σ^2 fixed at 0.004 Å^2 from ref 45. [c] σ^2 fixed at 0.005 Å^2 from ref 45.

TABLE 5: First Shell EXAFS Fit Results for Rh/C[a]

E, V vs RHE	N_{Rh-Rh}	R_{Rh-Rh}, Å	E_0, eV
0.30	7.75	2.683	−5.01
0.40	7.77	2.682	−5.06
0.50	7.63	2.681	−2.98
0.60	8.27	2.682	−3.26
0.70	8.23	2.682	−4.77
0.80	7.92	2.683	−5.56
0.90	7.63	2.683	−4.31
1.00	7.40	2.682	−4.62
1.10	7.24	2.684	−4.04
1.20	7.00	2.684	−3.97

[a] S_0^2 fixed at 0.921 as calculated via FEFF8.0, k range: 2.5−15 Å^{-1} (k^2), R range: 1.8−3.0 Å. Gross errors: $N \pm 20\%$, $R \pm 0.02$ Å. σ^2 fixed at 0.005 Å^2 from reported crystallographic data (JCPDF #01-1214).

Finally the dramatic increase in the magnitude of the N_{Rh-Rh} peak for the Rh_xS_y catalysts in 6 M TFMSA compared to in 1 M TFMSA (see Figure 7) suggests a quite different change in the Rh_xS_y catalyst in the presence of strong acid. The increase in the magnitude of N_{Rh-Rh} in concentrated 6 M TFMSA indicates the formation of a metallic Rh skin on the Rh_xS_y, and

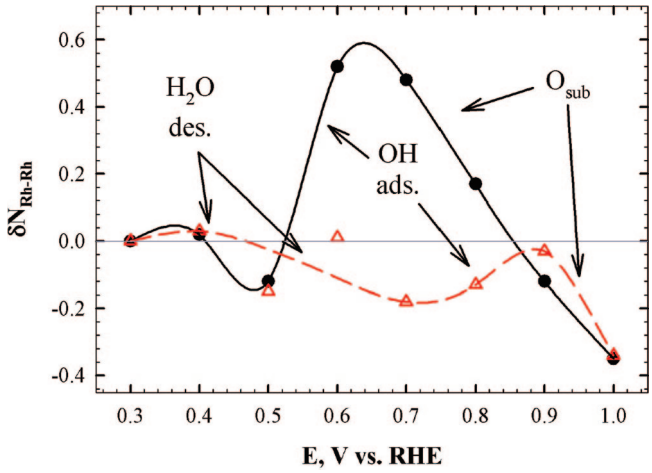

Figure 10. Plot of $\delta N_{Rh-Rh} = N_{Rh-Rh}(V) - N_{Rh-Rh}(0.30\ V)$ for Rh/C (●) and Rh_3S_4/C (Δ) in deaerated 1 M TFMSA. The processes responsible for the variations in δN are indicated and discussed in the text.

we suggest that S dissolution is primarily responsible. Analysis of the $\Delta\mu$ data below will confirm this.

The Rh_xS_y/C electrocatalyst was designed and optimized as an oxygen depolarized cathode (ODC) for electrolytic generation of chlorine gas from HCl feedstocks.[13,39] In this application, the cathode serves as a counter electrode to the important chlorine gas generating anode.[43,44] Reducing oxygen at the cathode lowers the overall cost of the process (by ca. 700 Wh kg^{-1} chlorine gas) and presents a safe alternative to the dangerous production of hydrogen gas. To perform ORR in O_2-saturated 5 M HCl at temperatures of 80 °C requires a material of exceptional stability. In a recent publication,[13] we evaluated Pt/C, Rh/C and traditional M_xRu_ySz/C (M = Co, Mo, Rh, or Re) chalcogenide electrocatalysts produced by the traditional nonaqueous method[15] for ODC applications. These materials immediately suffered irreversible dissolution under these harsh environments. For the traditional chalcogenides, the sulfur essentially forms loose adlayers on the surfaces of nanoscopic metal particles, which can be easily stripped from the particle surfaces.[4,13,17,40] In contrast, the De Nora Rh_xS_y/C electrocatalyst apparently forms a metallic layer in strong acid; albeit this layer is passivated with a layer of O(H) at nearly all potentials as we will see in the $\Delta\mu$ data. In the presence of HCl it is entirely possible that the metallic layer is covered with Cl ions in addition to the O(H) layer at some potentials, as is typical of Pt metal in the presence of Cl.[32,70] XAS studies of the Rh_xS_y catalyst in HCl[71] are currently underway.

3.4. Δμ Analysis. ***3.4.1. Theoretical Signatures.*** A proper interpretation of the experimental $\Delta\mu$ data below requires both an understanding of the change in magnitude and line shape with increase in electrochemical potential.[27,28,67] To understand the changes in line shape, the FEFF8.0 program[57] was utilized to produce theoretical XANES spectra from crystallographic models of the electrocatalyst. Based on the crystallographic properties of the three Rh−S phases in the balanced phase Rh_xS_y/C electrocatalyst (Table 1), our initial communications[3,37] centered on the metallic *C*2/*m* Rh_3S_4 phase. The clusters, and their corresponding FEFF8.0-calculated $\Delta\mu$ spectra, are presented in Figure 11. The left side of this Figure provides another elegant example of the crystallographic interrelationship of the Rh_2S_3 and Rh_3S_4 phase. As described above, Rh_3S_4 is essentially comprised of a Rh_2S_3 backbone of RhS_6 pseudo-octahedra. These octahedra are connected by a disulfide bridge with canted metallic Rh_6 octahedra to either side.[45] Both chemical intuition and the reported density of states determinations[45] designate these metallic Rh_6 clusters as the most likely active site for $O(H)_{ads}$.

Figure 11a−d shows the Rh_6 octahedra models utilized (with a "clean" cluster in the center) to generate the theoretical $\Delta\mu = \mu(Rh_6{-}O_{ads}) - \mu(Rh_6)$ curves at the bottom right. Figure 11a provides an example of 1-fold (i.e., "atop") O_{ads} on the Rh_6 cluster. Teliska et al., via density functional theory calculations,[28] showed that it is highly unlikely that molecular oxygen adsorption will occur via atop geometry, and this model therefore reflects the likely mode of either OH_{ads} resulting from water activation on the electrocatalyst surface or even of weakly chemisorbed H_2O.[33,35] Figure 11b−d shows modes of *n*-fold O_{ads} (bridge-bonded and 3-fold, respectively). Comparison of the FEFF8.0-calculated $\Delta\mu$ spectra to the experimentally derived spectra in the figures below will provide for an interpretation of the water activation process upon the different catalysts discussed in this work.

3.4.2. Δμ Spectra for Rh_xS_y/C. Figure 12 shows the XANES spectra (μ) before subtraction and the resultant differences, $\Delta\mu = \mu(V) - \mu(0.40\ V)$, for the Rh_xS_y/C electrocatalyst in deaerated 1 M TFMSA. The sensitivity of the $\Delta\mu$ difference technique is clearly indicated here. It is not until a potential of 1.00 V is reached that the Rh K edge XANES (Figure 12, left) exhibits a clearly visible increase in the white line (at least to the naked eye), but the $\Delta\mu$ show systematic differences and lineshapes similar to the theory in Figure 11. Note that the noise levels in these difference spectra (smoothed with a three-point (1.5 eV wide) Savitsky−Golay smoothing function) are still remarkably low. While it is impossible to state that the surface of the Rh_xS_y/C electrocatalyst is completely devoid of adsorbed species at 0.40 V, this potential represents the "cleanest" region between H_2O_{ads} and $O(H)_{ads}$ as we will show below. The surface sensitivity of the $\Delta\mu$ technique arises from the elimination of bulk, unreacting species from the XANES signals through normalized subtraction.

The $\Delta\mu$ results in Figure 12 for Rh_xS_y in 1 M TFMSA were the basis of our initial communications.[3,37] Below (Figures 13−15) we also present $\Delta\mu$ results for the Rh_2S_3, Rh_3S_4, Rh/C catalysts in 1 M TFMSA (and Rh_xS_y in 6 M TFMSA), to more fully understand the changes in the $\Delta\mu$ lineshapes. We also plot in Figure 16 the absolute magnitudes of the $\Delta\mu$ spectra around 0−3 eV to reflect the relative amount of O(H) on the surface. These magnitudes only qualitatively reflect the coverage because, as the coverage goes from atop OH to 3-fold O, the magnitudes of the $\Delta\mu$ signals per O adsorbate will change since the Rh−O coordination has changed. Further, the magnitudes of the $\Delta\mu$ will reflect the dispersion of the Rh in the various Rh clusters, and/or the extent of surface Rh atoms in the different RhS phases. Nevertheless, such a plot nicely summarizes the large amount of data (five catalysts at several potentials) making it possible to see the trends, and the qualitative fits given in Figure 16 enable a qualitative understanding of why these magnitudes vary as they do.

3.4.3. Interpretation of the Δμ Signatures. *a. Rh/C.* Comparison of the theoretical signatures and data in Figure 15 suggest predominantly atop OH below 0.7 V and *n*-fold O well above. The EXAFS in Figure 10 gives some evidence also for subsurface O above 1.0 V as discussed above.

b. Rh_3S_4. Comparison of the theoretical signatures and data in Figure 14 (right) suggests atop O at all potentials. We suggest that below 0.7 V the magnitudes in Figure 16 reflect H_2O

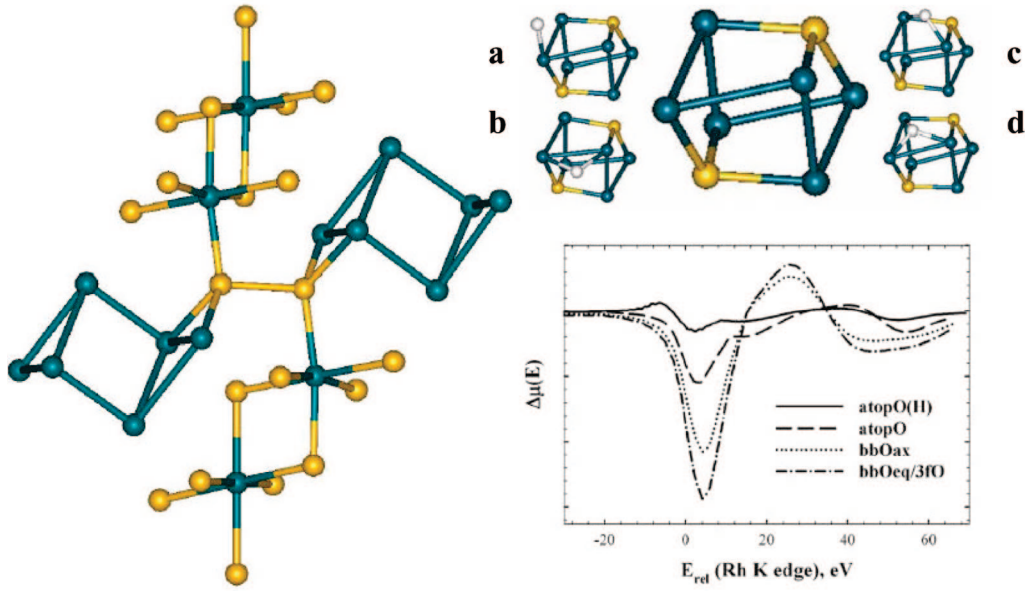

Figure 11. FEFF8.0-calculated $\Delta\mu = \mu(Rh_6S_2{-}O_{ads}) - \mu(Rh_6S_2)$ theory curves for *C*2/*m* Rh_3S_4 and the corresponding models. The rhodium and sulfur atoms are colored dark and light, respectively, with oxygen appearing as the white orb in the FEFF cluster fragments. Left: Rh_3S_4 fragment displaying the metallic Rh_6 octahedra to either side of the (Rh_2S_3) backbone; top right: Rh_6S_2 pseudo-octahedral clusters: (a) atopO, (b) axial bridge-bonded O (bbOax), (c) equatorial bridge-bonded O (bbOeq), (d) 3-fold O (3fO); center: clean cluster; bottom right: Rh K edge $\Delta\mu = \mu(Rh_6S_2{-}O_{ads}) - \mu(Rh_6S_2)$ signatures calculated with the FEFF8.0 code from the above clusters.

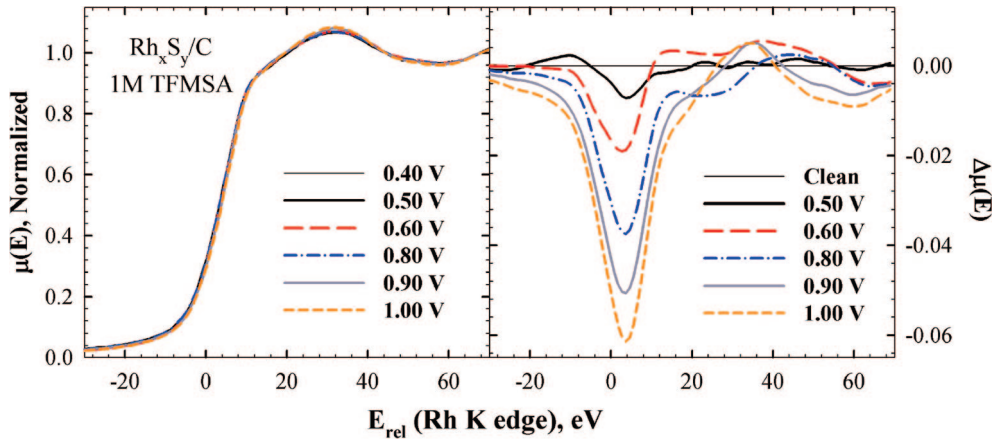

Figure 12. In situ Rh K edge XANES (left) and $\Delta\mu = \mu(V) - \mu(0.40\ V)$ (right) spectra for the De Nora 30 wt % Rh_xS_y/C electrocatalyst in deaerated 1 M TFMSA.

adsorption. This is strongly suggested by the lack of significant current flow below 0.7 V in the CV data shown on the graph, yet a significant $\Delta\mu$ intensity appears (current arises from oxidation, and chemisorbed water is not oxidized). Apparently a weakly bonded water double layer forms and then this double layer is disrupted prior to the adsorption of OH. We have seen this water double layer also on Pt in the potential range between 0.65 and 0.75 V with similar behavior (i.e., disruption before the onset of O(H)).[2,28] At 0.7 V all H_2O has desorbed and OH adsorbs above 0.7 V (see Figure 16).

c. Rh_2S_3. Again comparison with the theoretical signatures shown in Figure 14 suggests adsorption of atop O but which appears to convert to more *n*-fold O above 0.7 V. Consistent with the conclusions from the XRD, TEM and EXAFS analyses above, indicating that some Rh_2S_3 exists along with some small Rh metal particles, the $\Delta\mu$ is reflecting O(H)/Rh metal and some water on the Rh_2S_3 phase below 0.7 V. We estimate the components of each in Figure 16 by taking linear a combination of the $\Delta\mu$ water component on Rh_3S_4 (labeled 34° because it is only that part below 0.7 V) and the full O(H)/Rh metal $\Delta\mu$

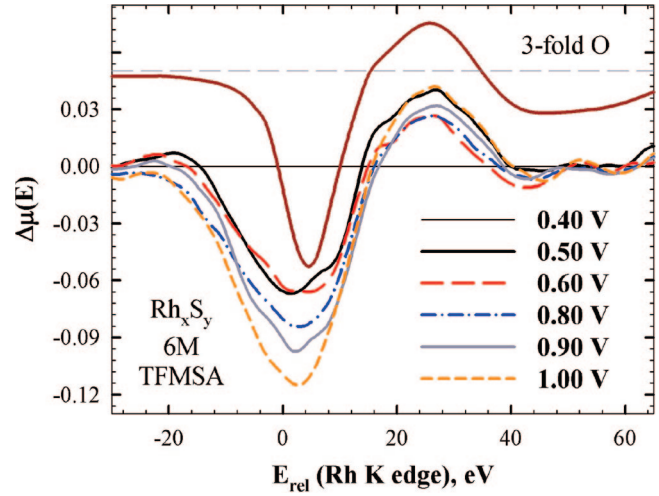

Figure 13. Experimental Rh K edge $\Delta\mu = \mu(V) - \mu(0.40\ V)$ spectra for Rh_xS_y/C in deaerated 6 M TFMSA (bottom) and comparison with theoretical *n*-fold O signature (top) from Figure 11.

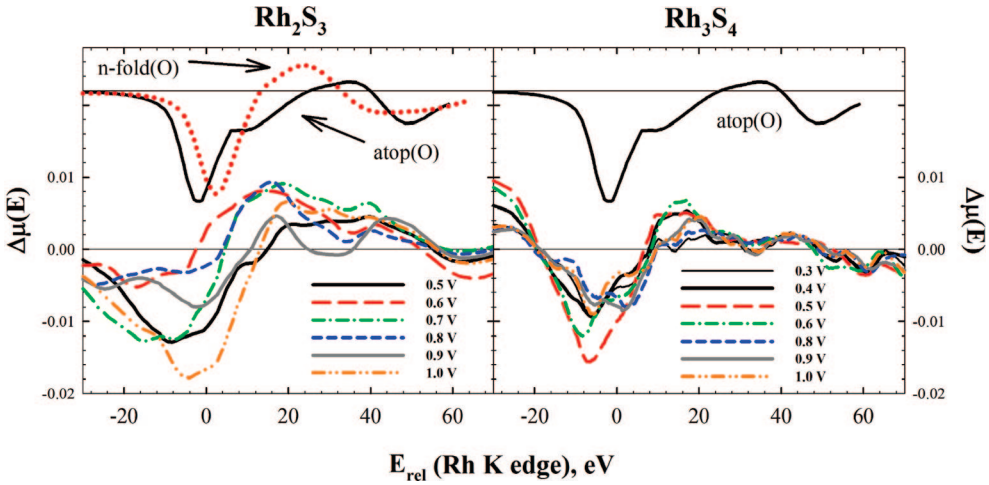

Figure 14. Rh K edge $\Delta\mu = \mu(V) - \mu(0.40\ V)$ signatures for the Rh_2S_3/C (left) and $\Delta\mu = \mu(V) - \mu(0.70\ V)$ for Rh_3S_4/C (right) preferential phases in deaerated 1 M TFMSA. The theoretical signatures for the indicated 3-fold O and atop O(H) moieties from Figure 11 are also indicated.

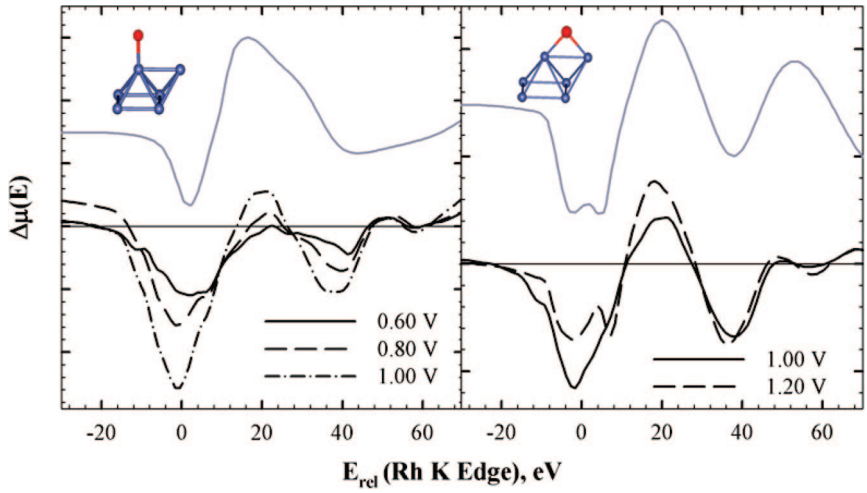

Figure 15. FEFF8.0-calculated $\Delta\mu = \mu(Rh_6{-}O_{ads}) - \mu(Rh_6)$ signals (gray) compared with experimental Rh/C $\Delta\mu$ spectra collected in situ in deaerated 1 M TFMSA: (left) atop O(H), (right) *n*-fold (bbO) signals.

amplitude, and determine the optimal linear fit. This fit is given in Figure 16 and denoted as 23 = .3*34° + .7*Rh, where we give only the *nm* indices to indicate the $\Delta\mu$ amplitude dependence for Rh_nS_m for brevity, and the numbers in front of the *nm* indicate the optimal coefficients. We believe the *n*-fold O comes from adsorption on Rh metal particles, as the Rh_2S_3 sample cannot dissociate water and only gives H_2O/Rh_2S_3 below 0.7 V.

d. Rh_xS_y in 1 M TFMSA. The experimental signatures in Figure 12 for Rh_xS_y indicate atop O below 0.7 V and then an increasing component of *n*-fold O above 0.7 V. The amplitude trend shown in Figure 16 is remarkably similar to that for Rh/C except a bit larger. The latter suggest we are just seeing O(H)/Rh, but that is not consistent with the $\Delta\mu$ signatures (i.e., the $\Delta\mu$'s for Rh_2S_3 and Rh/C are quite different). Therefore, we suggest we are seeing H_2O/Rh_xS_y and O(H)/Rh metal. A fit of the components suggest *xy* = 0.4*34 + 1.8*Rh. Note we do not use 34° here but 34 since we now used the amplitude over the entire range, below and above 0.7 V. We believe that some Rh_3S_4 phase is present in the Rh_xS_y sample so we use the entire amplitude trend to fit the Rh_xS_y trend in this case.

e. Rh_xS_y in 6 M TFMSA. Finally, the $\Delta\mu$ signatures for Rh_xS_y in 6 M TFMSA in Figure 13 suggests *n*-fold O at all potentials. We use the exact same components as for the Rh_xS_y in 1 M TFMSA and obtain the fit *xy* 6M/2 = 0.9*34° + 2.7*Rh. (Note, we write *xy* 6M/2 because the experimental amplitudes in Figure 16 have been divided by 2 to place it on the same curve in the figure; it is not clear why the amplitudes are so large for the *xy* 6M). The very large component of Rh metal now explains why the signature reflects *n*-fold O at all potentials (i.e., the Rh skin is more complete and thicker) and this layer is very reactive with *n*-fold O at all potentials.

3.4.4. Correlation of the $\Delta\mu$ Spectra with the Cyclic Voltammetry Results. Figure 16 also shows the magnitude of the CV curves from Figure 3 expanded in the range between 0.5 and 1.0 V. Above 0.7 V, the CV curves correlate with the component of Rh metal as found in the amplitude fits, that is the current follows the trend R*h* > 23 > *xy* >34. Recall that above 0.7 V, the $\Delta\mu$ amplitudes for the Rh_2S_3 preferential sample is dominated by the Rh metal component as the Rh_2S_3 phase above 0.7 V is actually inactive. The Rh_3S_4 phase has no O(H) present, except that from the huge Rh metal particles that have a smaller surface area, so the CV curve reflects the Rh_3S_4 phase with little oxidation. The Rh_xS_y sample has the Rh partial skin, so it shows an appreciable current.

Not shown in Figure 16, but evident in Figure 3, the onset of the lowest slope at low potentials begins at 0.4 V for all but the Rh_3S_4 sample, consistent with the $\Delta\mu$ amplitudes.

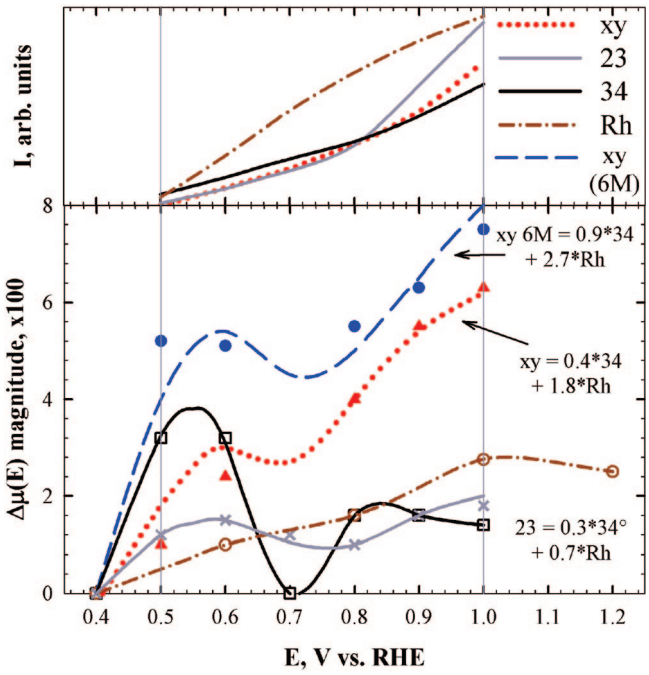

Figure 16. Plot of the $\Delta\mu$ amplitudes (between 0−3 eV) as a function of potential (denoted by the points) for the indicated Rh_nS_m catalysts (all in deaerated 1 M TFMSA except for that indicated in 6 M TFMSA) and the corresponding CV curves from Figure 3 (top). Lines through the points are the optimal linear fits of the indicated components with coefficients as discussed in the text. Lines for Rh/C and Rh_3S_4 are simply drawn through the points.

The onset Rh_3S_4 begins already at 0.25 consistent with the $\Delta\mu$ (we set it to zero at 0.4 in order to fit the other curves). Therefore, the CV data is completely consistent with the $\Delta\mu$ amplitudes, where the current comes primarily from water oxidation to OH and O, not chemisorbed water; however, the thresholds and low currents at the lowest potentials probably do come from some charge transfer between the chemisorbed H_2O and the Rh.

4. Summary and Conclusions

4.1. Water Activation and Stability in TFMSA.

Water activation behavior can be summarized as follows: (a) OH adsorption occurs well below 0.75 V on Rh/C. This is not surprising because pure Rh is very reactive and can dissociate water well below 0.75 V. However, the huge 100 nm particles are much less reactive. (b) Water dissociation does not occur at all on the Rh_2S_3 and only above 0.75 V on the Rh_3S_4. The small amount of *n*-fold O(H) seen well above 0.75 V in the Rh_2S_3 case we believe occurs due to the smaller Rh particles resulting from the heating. (c) The $\Delta\mu$ amplitude trends for the Rh_2S_3 and Rh_3S_4 are very different from that for Rh. This suggests strongly that the Rh_2S_3 and Rh_3S_4 are stable to the 1 M TFMSA. In contrast, the $\Delta\mu$ amplitude trend for the Rh_xS_y is remarkably similar to that for Rh/C, except for the larger overall magnitude (although the signatures for Rh and Rh_xS_y are quite different). This suggests that a very thin layer of Rh lies over the Rh_xS_y sample (i.e., S dissolution also occurred in the 1 M but less so). Its presence is not visible in the N_{Rh-Rh} EXAFS because of the very thin layer, but is indeed visible in the data for Rh_xS_y in the 6 M TFMSA as discussed above.

4.2. ORR Reactivity.

The ORR reactivity can be summarized as below: (a) The ORR reactivity on all samples takes off only below 0.75 V. This is where all $\Delta\mu$ data and the CV's show a second onset (Figure 16), and this onset arises from O(H) adsorption. Therefore, O(H) adsorption (oxidation) clearly poisons ORR on RhS and O oxide formation on Rh. (b) OH adsorption occurs well below 0.75 V on Rh as stated above, because Rh is very reactive. Indeed this OH is now needed to "tame" the reactivity of Rh so that ORR can occur. In this regard, the ORR on Rh is not that different from ORR on the RhS samples, except now the Rh is "tamed" by the O(H) rather than by the S. It would appear partial coverage of the Rh surface by the OH is needed, but when it goes subsurface to form the oxide, the reactivity ceases (hence its onset at 0.75 V). (c) The ORR reactivity of the Rh_3S_4 sample apparently is occurring on the small Rh_6 moieties present in the crystalline Rh_3S_4 sample. (d) The ORR reactivity on the Rh_xS_y could be occurring either because of the presence of the Rh_3S_4 phase or Rh metal on the surface or both. The $\Delta\mu$ data suggest a Rh layer at the surface as described above, but certainly the Rh_3S_4 phase can also contribute. The component fits to the amplitude curve reflect water activation on both, and ORR on both is clearly occurring (the Rh_3S_4 sample is equally ORR reactive). (e) The apparent greater Tafel slope for the Rh_2S_3 and Rh_3S_4 samples could arise from a number of factors: (1) increasing coverage of water seen directly in the $\Delta\mu$ as the potential decreases, (2) larger resistance in the cell, or (3) a different charge transfer mechanism (i.e., a different charge transfer coefficient). In the first mechanism chemisorbed water slows the exchange rate of the rds in the ORR. The fact that the slope for the Rh and Rh_xS_y is similar gives more evidence for the importance of the Rh surface layer on the Rh_xS_y clusters and that it could be dominating the ORR. In mechanism 2, the Rh−S phases have larger resistance than the Rh metal (Rh/C or the Rh skin on the Rh_xS_y sample). Finally, it is possible that the charge transfer coefficient is simply a bit larger for the Rh_2S_3 and Rh_3S_4 samples, reflecting a slightly different point where the electron transfer occurs.

4.3. Conclusions.

Finally, the following general conclusions can be drawn: (a) Heating causes Rh segregation and the formation of Rh metal particles. TFMSA causes S dissolution and the formation of a Rh skin on the Rh_xS_y samples, but not on the Rh_2S_3 and Rh_3S_4 preferential samples (the prior heating process has made them stable to TFMSA). (b) At least some Rh−Rh interaction is needed to carry out the ORR. This is present in the Rh_3S_4 sample on the Rh_6 moieties in the sample, and Rh_3S_4 is present in the Rh_xS_y sample, but the Rh skin resulting from dissolution of S in the TFMSA may be (probably is) dominating in this case. However, the Rh_3S_4 preferential sample is nearly equally reactive for the ORR.

This report builds on the initial XANES $\Delta\mu$ studies[3,37] of the mixed-phase Rh_xS_y/C (De Nora) chalcogenide electrocatalyst system, which yielded preliminary information regarding the water activation pathway via theoretical investigations of the metallic Rh_3S_4 phase. In the present report, a more comprehensive picture is presented using preferential phases Rh_2S_3 and Rh_3S_4. These results indicate that our previous conclusions were correct, and that Rh_3S_4 serves as the active phase in the Rh_xS_y electrocatalyst system. As indicated earlier, the metallic Rh_6 octahedra in the Rh_3S_4 serve as an active site for ORR. However, the results of the 6 M TFMSA study indicate that Rh_3S_4 has an additional active site: a metallic self-generating Rh layer. While

both phases are active for ORR, the results indicate that the brunt of the reactivity is attributable to the metallic Rh layer. Direct spectroscopic observation of these dual sites was accomplished through the application of the $\Delta\mu$ technique of XANES analysis to *in operando* catalyst systems.

Acknowledgment. Financial and intellectual support was provided by the De Nora R&D Division, in particular, Robert J. Allen, and is registered with the Office of Patents and Trademarks under the following numbers: US 6,967,185, US 6,149,782, and U.S. 6,358,381. Further support was supplied from the Army Research Office under the auspices of a Multi-University Research Initiative lead by Case Western Reserve University (Contract No. DAAD19-03-1-0169). The use of beamlines X-7B and X-18B at the National Synchrotron Light Source, Brookhaven National Laboratory, was supported by the U.S. Department of Energy, Office of Science, Office of Basic Energy Sciences, under Contract No. DE-AC02-98CH10886.

Supporting Information Available: Figures showing the electrochemical response of the Rh/C, Rh_xS_y/C, Rh_2S_3/C, and Rh_3S_4/C electrodes during the in situ XAS experiments accompanied by a brief explanation of the experimental conditions. This material is available free of charge via the Internet at http://pubs.acs.org.

References and Notes

(1) Ross, P. N. The Science of Electrocatalysis on Bimetallic Surfaces In *Electrocatalysis*; Lipkowski, J., Ross, P. N., Eds.; Wiley-VCH: New York, 1998; p 43.

(2) Teliska, M.; Murthi, V. S.; Mukerjee, S.; Ramaker, D. E. *J. Electrochem. Soc.* **2005**, *152*, A2159.

(3) Ziegelbauer, J. M.; Gatewood, D.; Gullá, A. F.; Ramaker, D. E.; Mukerjee, S. *Electrochem. Solid-State Lett.* **2006**, *9*, A430.

(4) Ziegelbauer, J. M.; Murthi, V. S.; O'Laoire, C.; Gullá, A. F.; Mukerjee, S. *Electrochim. Acta* **2008**, *53*, 5587.

(5) Ziegelbauer, J. M.; Olson, T. S.; Pylypenko, S.; Alamgir, F.; Jaye, C.; Atanassov, P.; Mukerjee, S. *J. Phys. Chem. C* **2008**, *112*, 8839.

(6) Alonso-Vante, N. Novel nanostructured material based on transition-metal compounds for electrocatalysis. In *Catalysis and Electrocatalysis at Nanoparticle Surfaces*; Wieckowski, A., Savinova, E. R., Vayenas, C. G. , Eds.; Marcel Dekker: New York, 2003; p 931.

(7) Vante, N. A.; Tributsch, H. *Nature* **1986**, *323*, 431.

(8) González-Huerta, R. G.; Chávez-Carvayar, J. A.; Solorza-Feria, O. *J. Power Sources* **2006**, *153*, 11.

(9) Shukla, A. K.; Raman, R. K. *Annu. Rev. Mater. Res.* **2003**, *33*, 155.

(10) Reeve, R. W.; Christensen, P. A.; Dickinson, A. J.; Hamnett, A.; Scott, K. *Electrochim. Acta* **2000**, *45*, 4237.

(11) Reeve, R. W.; Christensen, P. A.; Hamnett, A.; Haydock, S. A.; Roy, S. C. *J. Electrochem. Soc.* **1998**, *145*, 3463.

(12) Tributsch, H.; Bron, M.; Hilgendorff, M.; Schulenburg, H.; Dorbandt, I.; Eyert, V.; Bogdanoff, P.; Fiechter, S. *J. Appl. Electrochem.* **2001**, *31*, 739.

(13) Ziegelbauer, J. M.; Gullá, A. F.; O'Laoire, C.; Urgeghe, C.; Allen, R. J.; Mukerjee, S. *Electrochim. Acta* **2007**, *52*, 6282.

(14) Schulenburg, H.; Hilgendorff, M.; Dorbandt, I.; Radnick, J.; Bogdanoff, P.; Fiechter, S.; Bron, M.; Tributsch, H. *J. Power Sources* **2005**, *155*, 47.

(15) Solorza-Feria, O.; Ellmer, K.; Giersig, M.; Alonso-Vante, N. *Electrochim. Acta* **1994**, *39*, 1647.

(16) Bastide, S.; Levy-Clement, C.; Albu-Yaron, A.; Boucher, A. C.; Alonso-Vante, N. *Electrochem. Solid-State Lett.* **2000**, *3*, 450.

(17) Dassenoy, F.; Vogel, W.; Alonso-Vante, N. *J. Phys. Chem. B* **2002**, *106*, 12152.

(18) Fan, Q.; Pu, C.; Ley, K. L.; Smotkin, E. S. *J. Electrochem. Soc.* **1996**, *143*, L21.

(19) Fan, Q.; Pu, C.; Smotkin, E. S. *J. Electrochem. Soc.* **1996**, *143*, 3053.

(20) Marković, N. M.; Lucas, C. A.; Rodes, A.; Stamenković, V.; Ross, P. N. *Surf. Sci.* **2002**, *499*, L149.

(21) Stamenković, V. C.; Arenz, M.; Lucas, C. A.; Gallagher, M. E.; Ross, P. N.; Marković, N. M. *J. Am. Chem. Soc.* **2003**, *125*, 2736.

(22) Villegas, I.; Weaver, M. J. *J. Chem. Phys.* **1994**, *101*, 1648.

(23) Christensen, P. A.; Hamnett, A.; Weeks, S. A. *J. Electroanal. Chem.* **1998**, *250*, 127.

(24) Mukerjee, S. In-Situ X-Ray Absorption Spectroscopy of Carbon-Supported Pt and Pt-Alloy Electrocatalysts: Correlation of Electrocatalytic Activity with Particle Size and Alloying In *Catalysis and Electrocatalysis at Nanoparticle Surfaces*; Wieckowski, A., Savinova, E. R., Vayenas, C. G., Eds.; Marcel Dekker: New York, 2003; p 501.

(25) McBreen, J.; O'Grady, W. E.; Pandya, K. I.; Hoffman, R. W.; Sayers, D. E. *Langmuir* **1987**, *3*, 428.

(26) Russell, A. E.; Maniquet, S.; Mathew, R. J.; Yao, H.; Roers, M. A.; Thompsett, D. *J. Power Sources* **2001**, *96*, 226.

(27) Teliska, M.; O'Grady, W. E.; Ramaker, D. E. *J. Phys. Chem. B* **2004**, *108*, 2333.

(28) Teliska, M.; O'Grady, W. E.; Ramaker, D. E. *J. Phys. Chem. B* **2005**, *109*, 8076.

(29) Roth, C.; Benker, N.; Buhrmester, T.; Mazurek, M.; Loster, M.; Fuess, H.; Koningsberger, D. C.; Ramaker, D. E. *J. Am. Chem. Soc.* **2005**, *127*, 14607.

(30) Scott, F. J.; Mukerjee, S.; Ramaker, D. E. *J. Electrochem. Soc.* **2007**, *154*, A396.

(31) Teliska, M.; Murthi, V. S.; Mukerjee, S.; Ramaker, D. E. *J. Phys. Chem. C* **2007**, *111*, 9267.

(32) Arruda, T. M.; Shyam, B.; Ziegelbauer, J. M.; Mukerjee, S.; Ramaker, D. E. *J. Phys. Chem. C* **2008**, *112*, 18087–18097.

(33) Murthi, V. S.; Urian, R. C.; Mukerjee, S. *J. Phys. Chem. B* **2004**, *108*, 11011.

(34) Anderson, A. B.; Neshev, N. M.; Sidik, R. A.; Shiller, P. *Electrochim. Acta* **2002**, *47*, 2999.

(35) Anderson, A. B.; Roques, J.; Mukerjee, S.; Murthi, V. S.; Markovic, N. M.; Stamenkovic, V. *J. Phys. Chem. B* **2005**, *109*, 1198.

(36) Mukerjee, S.; Urian, R. C. *Electrochim. Acta* **2002**, *47*, 3219.

(37) Ziegelbauer, J. M.; Gatewood, D.; Ramaker, D. E.; Mukerjee, S. *ECS Trans.* **2006**, *1*, 119.

(38) Bayer charges ahead with novel cathode ChemicalProcessing.com, accessed 2006.

(39) Gullá, A. F.; Gancs, L.; Allen, R. J.; Mukerjee, S. *Appl. Catal. A* **2007**, *326*, 227.

(40) Cao, D.; Wieckowski, A.; Inukai, J.; Alonso-Vante, N. *J. Electrochem. Soc.* **2006**, *153*, A869.

(41) Johnson-Matthey. *The Platinum Metals Report: May 2008*; www.platinum.matthey.com, **2008**

(42) Papageorgopoulos, D. C.; Liu, F.; Conrad, O. *Electrochim. Acta* **2007**, *52*, 4982.

(43) Gestermann, F. Oxygen Depolarized Cathodes in the Chlor Alkali Electrolysis—On the Way to Industrial Application; *Electrolysis in the Chemical Industry*; 1998.

(44) Gestermann, F.; Ottaviani, A. *Mod. Chlor-Alkali Tech.* **2001**, *8*, 49.

(45) Beck, J.; Hilbert, T. *Z. Anorg. Allg. Chem.* **2000**, *626*, 72.

(46) Geller, S. *Acta Crystallogr.* **1962**, *15*, 1198.

(47) Parthe, E.; Hohnke, D. K.; Hulliger, F. *Acta Crystallogr.* **1967**, *23*, 832.

(48) Enayetullah, M. A. The Role of Electrolyte in Oxygen Electroreduction Catalysis Ph.D. Thesis; Case Western Reserve University: Cleveland, OH, 1986.

(49) Allen, R. J. ; Giallombardo, J. R. ; Czerwiec, D. ; De Castro, E. S.; Shaikh, K. Rhodium electrocatalyst and method of preparation; De Nora S.p.A: US, 2000; pp 14.

(50) Allen, R. J. ; Giallombardo, J. R. ; Czerwiec, D. ; De Castro, E. S.; Shaikh, K. Rhodium electrocatalyst and method of preparation; De Nora S.p.A.: U.S., 2002.

(51) Allen, R. J. ; Gullá, A. F. Synthesis of noble metal sulfide catalysts in a sulfide ion-free aqueous environment; De Nora Elettrodi S.p.A.: U.S., 2005; p 15.

(52) Enayetullah, M. A.; DeVilbiss, T. D.; Bockris, J. O. M. *J. Electrochem. Soc.* **1989**, *136*, 3369.

(53) Paulus, U. A.; Schmidt, T. J.; Gasteiger, H. A.; Behm, R. J. *J. Electroanal. Chem.* **2001**, *495*, 134.

(54) Bard, A. J.; Faulkner, L. F. *Electrochemical Methods: Fundamentals and Applications*, 2nd ed.; Wiley: New York, 2001.

(55) Newville, M. *J. Synchrotron. Radiat.* **2001**, *8*, 322.

(56) Chen, M. H.; Crasemann, B.; Mark, H. *Phys. Rev. A* **1981**, *24*, 177.

(57) Ankudinov, A. L.; Ravel, B.; Rehr, J. J.; Conradson, S. D. *Phys. Rev. B* **1998**, *58*, 7565.

(58) Horanyi, G.; Rizmayer, E. M. *J. Electroanal. Chem.* **1986**, *198*, 379.

(59) Hourani, M.; Weickowski, A. *J. Electroanal. Chem.* **1988**, *244*, 147.

(60) Marković, N. M.; Ross, P. N. *Surf. Sci. Rep.* **2002**, *45*, 117.

(61) Damjanovic, A.; Brusic, V. *Electrochim. Acta* **1967**, *12*, 615.

(62) Damjanovic, A.; Grenshaw, M. A.; Bockris, J. O. M. *J. Phys. Chem.* **1966**, *70*, 3761.

(63) Koningsberger, D. C.; Mojet, B. L.; van Dorssen, G. E.; Ramaker, D. E. *Top. Catal.* **2000**, *10*, 143.

(64) Mukerjee, S.; Srinivasan, S.; Soriaga, M. P.; McBreen, J. *J. Phys. Chem.* **1995**, *99*, 4577.

(65) Nagata, S.; Atake, T. *J. Therm. Anal. Calorim.* **1999**, *57*, 807.

(66) Janin, E.; von Schenck, H.; Göthelid, M.; Karlsson, U. O. *Phys. Rev. B* **2000**, *61*, 13144.

(67) Ramaker, D. E.; Koningsberger, D. C. *Phys. Rev. Lett.* **2002**, *89*, 139701.

(68) Garsany, Y.; Baturina, O. A.; Swider-Lyons, K. *J. Electrochem. Soc.* **2007**, *154*, B670.

(69) Gatewood, D. S.; Schull, T. L.; Baturina, O. A.; Pietron, J. J.; Garsany, Y.; Swider-Lyons, K.; Ramaker, D. E. *J. Phys. Chem. B* **2008**, *112*, 4961.

(70) Schmidt, T. J.; Paulus, U. A.; Gasteiger, H. A.; Behm, R. J. *J. Electroanal. Chem.* **2001**, *508*, 41.

(71) Korovina, A.; Ziegelbauer, J. M.; Mukerjee, S.; Ramaker, D. E. manuscript in preparation.

JP809296X